

Setting the photoelectron clock through molecular alignment

Andrea Trabattoni,^{1,2} Joss Wiese,^{1,3} Umberto De Giovannini,^{4,5} Jean-François Olivieri,¹ Terry Mullins,¹ Jolijn Onvlee,¹ Sang-Kil Son,^{1,2} Biagio Frusteri,⁵ Angel Rubio,^{4,6,7} Sebastian Trippel,^{1,2} and Jochen Küpper^{1,2,3,7}

¹*Center for Free-Electron Laser Science, Deutsches Elektronen-Synchrotron DESY, Notkestraße 85, 22607 Hamburg, Germany*

²*The Hamburg Center for Ultrafast Imaging, Universität Hamburg, Luruper Chaussee 149, 22761 Hamburg, Germany*

³*Department of Chemistry, Universität Hamburg, Martin-Luther-King-Platz 6, 20146 Hamburg, Germany*

⁴*Max Planck Institute for the Structure and Dynamics of Matter and*

Center for Free-Electron Laser Science, 22761 Hamburg, Germany

⁵*Dipartimento di Fisica e Chimica, Università degli Studi di Palermo, Via Archirafi 36, I-90123, Palermo, Italy*

⁶*Center for Computational Quantum Physics (CCQ), The Flatiron Institute, 162 Fifth Avenue, New York NY 10010*

⁷*Department of Physics, Universität Hamburg, Luruper Chaussee 149, 22761 Hamburg, Germany*

(Dated: April 20, 2020)

The interaction of strong laser fields with matter intrinsically provides powerful tools to image transient dynamics with an extremely high spatiotemporal resolution. Here, we study strong-field ionisation of laser-aligned molecules and show a full real-time picture of the photoelectron dynamics in the combined action of the laser field and the molecular interaction. We demonstrate that the molecule has a dramatic impact on the overall strong-field dynamics: it sets the clock for the emission of electrons with a given rescattering kinetic energy. This result represents a benchmark for the seminal statements of molecular-frame strong-field physics and has strong impact on the interpretation of self-diffraction experiments. Furthermore, the resulting encoding of the time-energy relation in molecular-frame photoelectron momentum distributions shows the way of probing the molecular potential in real-time and accessing a deeper understanding of electron transport during strong-field interactions.

INTRODUCTION

In the prototypical strong-field interaction, an intense driving field extracts a valence electron from the target through tunnel ionisation, accelerates the free electron in vacuum, and eventually drives it back to the parent ion, predominantly resulting in rescattering or radiative recombination [1, 2]. The radiative recombination results in the emission of high-energy photons by high-harmonic generation [1] and this is a powerful tool to investigate the electronic structure with attosecond temporal resolution [3–5]. Alternatively, the rescattered portion of this electron wavepacket is exploited in laser-induced electron diffraction (LIED) [6] experiments as a coherent diffraction pattern of the molecular target, potentially providing time-dependent images of the molecule at sub-femtosecond and few-picometer resolution. Recently, corresponding experimental results for the structure or dynamics of small or highly-symmetric molecules were obtained [7–12]. At the same time, the initial conditions of the strong-field interaction have attracted much attention for capturing the intrinsic nature of strong-field physics.

While pioneering attosecond experiments and molecular-frame measurements revealed non-trivial spatiotemporal features in electron tunnelling [13, 14], these initial conditions are still generally considered a weak perturbation in strong-field physics. All the results obtained in LIED experiments, for example, are interpreted in the framework of the strong-field approximation, where the electron is considered to be born in the continuum with a negligible initial momentum and to propagate as a plane wave [15]. Furthermore, the

post-ionisation dynamics before rescattering are assumed to be fully driven by the laser field, by neglecting, for example, the Coulomb interaction with the ionised molecule.

Common strategies to analyse photoelectron momentum distributions rely on the quantitative rescattering theory (QRS) [15], where angular dependence in the final photoelectron wavepacket is introduced solely through rescattering. Within this approach, diffraction patterns were analysed utilising the angular [7, 8] or radial [16] photoelectron distribution. However, the relevance of the ionised molecular orbital in the rescattered photoelectrons is still under discussion [17]. So far, this was included by an overall weighting factor in the rescattering probability [18, 19], or as a spatial phase or an angular feature in the rescattering electron wavepacket [14, 20]. Recently, the influence of molecular alignment on molecular structure retrieval was discussed [16, 21]. However, general predictions are still extremely challenging with new models appearing [22, 23].

Here, we experimentally and computationally study molecular-frame photoelectron spectroscopy from strongly aligned molecules in order to investigate the relation between the molecular frame and the strong-field-induced ultrafast electron dynamics. We demonstrate that and how the molecular frame governs the rescattering time for the photoelectron and, consequently, its final kinetic energy.

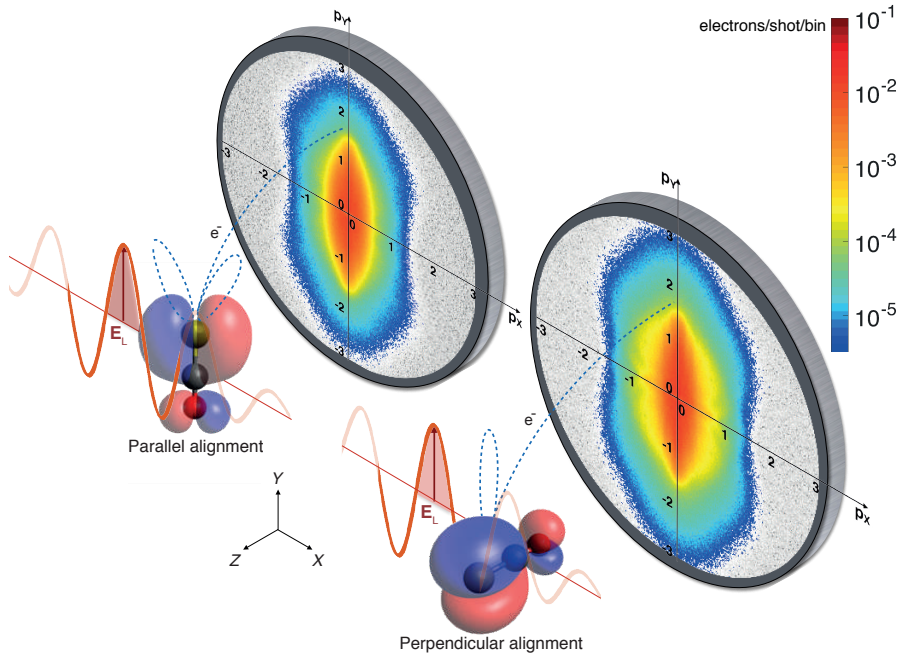


FIG. 1. Sketch of the experimental arrangement. OCS molecules (O in red, C in black, S in yellow) were aligned in the laboratory frame, parallel and perpendicular to the Y axis. The ionising laser electric field (\mathbf{E}_L) was linearly polarised along the Y axis and the detection was in the XY plane. The molecular-frame angle-resolved photoelectron spectra were projected onto a 2D detector in a velocity-map-imaging spectrometer. The alignment-dependent photoelectron trajectories are pictorially shown (blue dashed lines), as well as the corresponding shape of the ionising orbital (blue and red lobes). The spectra are displayed on a logarithmic intensity scale in units of electrons/shot/bin.

RESULTS

Experimental approach

Fig. 1 depicts the experiment. An ensemble of carbonyl sulphide (OCS) molecules all in the rovibronic ground state [24] was adiabatically aligned in the laboratory frame, with $\langle \cos^2 \theta_{2D} \rangle = 0.9$, by using a linearly polarised, 500 ps laser pulse, centred at 800 nm [25, 26], with a peak intensity $I = 3 \times 10^{11} \text{ W cm}^{-2}$. The molecules were aligned in two different configurations, shown in Fig. 1, with the molecular axis along the Y and Z axes, named parallel and perpendicular alignment, respectively. A second laser pulse, centred at 1300 nm, with a duration of 65 fs, and a peak intensity $I = 8 \times 10^{13} \text{ W cm}^{-2}$, was used to singly ionise the OCS molecules. For this intensity the ponderomotive energy of the laser field is $U_p \approx 13 \text{ eV}$ and the ionisation occurred in the tunnelling regime. The electric field of the ionising laser pulse, \mathbf{E}_L in Fig. 1, was linearly polarised along the Y axis (ellipticity $\epsilon = I_Z/I_Y < 0.005$). The produced molecular-frame angle-resolved photoelectron spectra (MF-ARPES) were recorded in a velocity map imaging (VMI) spectrometer [27] with its detector parallel to the XY plane. It is important to note that the de Broglie wavelength of rescattering electrons in the experiment was larger than 200 pm. In this regime no diffraction feature is expected

to appear in the photoelectron distributions [16].

Photoelectron-momentum distributions

Fig. 1 shows the MF-ARPES for parallel (left) and perpendicular (right) alignment. The two distributions show several differences. The spectrum for parallel alignment has a larger width at small transverse momenta, $p_X < 0.5 \text{ a. u.}$ (atomic units), while the spectrum for perpendicular alignment shows a number of angular features for transverse momenta p_X between 0.5 a. u. and 1 a. u.. These angular structures, which are much weaker in the spectrum for parallel alignment, could be identified as forward-rescattering features [28]. Focussing the attention on large longitudinal momenta p_Y , the counts for parallel alignment drop around 2.5 a. u.. In the case of perpendicular alignment, however, the spectrum extends to larger momenta, showing an appreciable amount of counts at $p_Y = 3 \text{ a. u.}$ Following the strong-field approximation, the hard cutoff of photoelectron momentum is expected to only depend on the properties of the laser field [29]. Experimentally, this quantity is hard to measure. Thus, the turning-point of the signal drop, i. e., the minimum of the first derivative, at large longitudinal momenta is used instead. In the following, we use the term cutoff in the latter sense. Surprisingly, in the current study we found

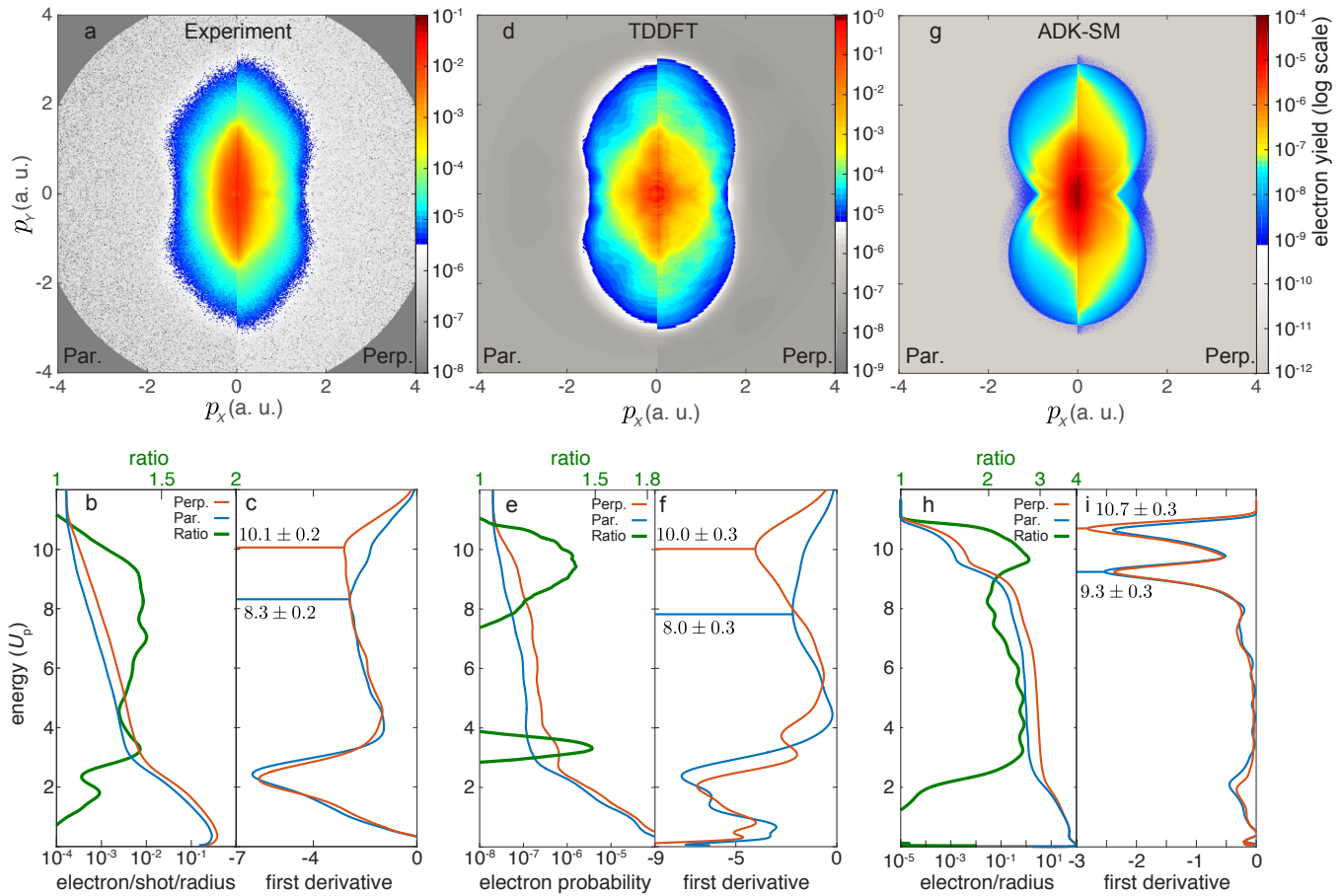


FIG. 2. Molecular-frame angle-resolved photoelectron spectra of OCS. These data were obtained **a, b, c** experimentally and computationally from **d, e, f** TDDFT and **g, h, i** ADK-SM calculations. **a, d, g**: Split graphical representation as a comparison of the photoelectron distributions for parallel and perpendicular alignment for the experimental and computational results, respectively. **b, e, h**: Corresponding projected energy distributions of photoelectrons along the Y axis, angularly integrated within a cone of $\pm 20^\circ$, as well as the ratio of the integral-normalised perpendicular and parallel distributions, on logarithmic scales. Energies are reported in units of the ponderomotive energy U_p . **c, f, i**: First derivatives of the photoelectron-energy distributions to evaluate the high-energy cutoff for the two molecular-alignment cases. All TDDFT computational results were obtained by averaging over different laser-molecule orientations according to the experimental alignment distributions and by adding a constant to account for the experimental background level. The ADK-SM results refer to a single laser intensity and perfect alignment for both cases. See Appendix B for details.

a clear dependence of the cutoff on the molecular frame.

Fig. 2 a shows a close comparison of the two experimental distributions for the complete range of p_X and p_Y , between 0 and 4 a.u. Here, the spectra were split along the Y axis and the spectrum from parallel alignment is shown on the left and the one from perpendicular alignment on the right. Now, the differences at small momenta as well as at the cutoff are even more evident. To perform a quantitative analysis of the cutoffs, the momentum distributions were angularly integrated within a cone of $\pm 20^\circ$ with respect to the longitudinal axis (Y) and converted to an energy scale. In Fig. 2 b the resulting photoelectron spectra are shown for parallel (blue) and perpendicular (red) alignment, with energies in units of U_p . The perpendicular/parallel ratio of the

two area-normalised spectra (green) shows a predominance of photoelectrons for perpendicular alignment in the energy range between $2 U_p$ and $10 U_p$, where the distribution is dominated by rescattered electrons [30]. Furthermore, the ratio increases with energy, reaching the maximum around the cutoff. To evaluate the cutoffs, the first derivative of the energy distributions are shown in Fig. 2 c and their minima were used to find the edges of the distributions, which allowed us to analyse the cutoff region. The first minimum represents the drop of direct electrons [30] and it was around $2 U_p$ for both alignment cases. This excluded any significant alignment-dependent direct-electron-cutoff enhancement [31]. Surprisingly, the second minimum behaves differently for the two alignments. While it is located around $10 U_p$ for perpendicular

alignment, as expected from the well established above-threshold ionisation theory [29], the cutoff is shifted down to a value around $8.5 U_p$ for parallel alignment.

Quantum-mechanical model of the electron dynamics

To unravel the experimental observations, state-of-the-art calculations were performed using both, time-dependent density-functional theory (TDDFT) [32] and a semiclassical molecular trajectory simulation setup. Using TDDFT, the MF-ARPES probability was calculated by simulating the complete dynamics of the many-body ionisation process in real-time and real-space with the tSURFF method [33, 34], see Appendix A for details. With this technique the spectrum was obtained by computing the entire time-dependent electron dynamics, including many-body electron interactions, and collecting the flux of electrons through a closed surface surrounding the molecule. Fig. 2 d, e, f report the same analysis of the numerical results as performed for the experimental data in Fig. 2 a, b, c. The simulations capture the principal features of experimental data very well. In particular, Fig. 2 f shows that the calculations reproduce the experimental cutoff positions for parallel and perpendicular alignment as well as the corresponding shift between them very well. This result is strongly affected by the electron-electron interaction and the interplay between different orbitals. Indeed, it is evident from the calculation that the molecule is predominantly ionised from the highest-occupied molecular orbital (HOMO) for both alignments. In the case of parallel alignment, nevertheless, a small contribution of HOMO-1 to the yield of high-energy rescattered electrons is observed. When the electron-electron interaction is artificially turned off the HOMO-1 contribution becomes significant and in this scenario the reduced cutoff observed in the experiment is not reproduced, see Supplementary Figure 4. Instead, in the case of fully interacting electrons the yield of the rescattered electrons ionised from HOMO-1 is suppressed, resulting in the really good agreement with the experiment.

Semiclassical model of the electron dynamics

Furthermore, semiclassical trajectory simulations based on the Ammosov-Delone-Kraïnov (ADK) tunnelling theory [35] in conjunction with a simple man propagation (SM) [36, 37] were conducted in order to track the molecular-frame electron dynamics during the strong-field interaction [38], see Appendix B for details. Based on the TDDFT analysis of the different molecular orbitals contributing to the photoelectron dynamics, the ionisation was assumed to occur solely from HOMO. In the underlying model, the initial phase-space distribution

of the electron wavepacket in the continuum at birth was described by the quasistatic ADK tunnelling theory, and the nodal structure of the HOMO was accounted for as imprint onto this initial momentum distribution. Post-ionisation dynamics of the electron wavepacket were evaluated in the combined interaction with the laser electric field and the cation's Coulomb field modelled as a point charge. To evaluate the accuracy of this semiclassical description, the resulting MF-ARPES for parallel and perpendicular alignment were calculated and analysed, see Fig. 2 g, h, i, and they show a really good agreement, both, with the experimental data and the full TDDFT calculation, reproducing the main features and cutoffs observed in the experiment very well. In particular, as seen by the local maximum around $10 U_p$ of the ratio of the two alignment cases, Fig. 2 h, this semiclassical model captures the enhanced yield of high-energy rescattered electrons for perpendicular alignment with respect to parallel alignment. This result is corroborated by the enhanced cutoff around $10.7 U_p$ for perpendicular alignment in Fig. 2 i, although a smaller yield at this energy is present also for parallel alignment. In addition, a relevant minimum appears around $9.3 U_p$ for both alignments. These features of ADK-SM, together with the pronounced yield along the centreline of Fig. 2 g, are known to be mainly due to Coulomb focussing [39], i. e., the dynamics of a continuum electron wavepacket being focussed along a perfectly linear laser polarisation axis. The relevance of this effect is discussed further below.

Differential analysis of the momentum distributions

To obtain a more comprehensive picture of the alignment-dependent photoelectron dynamics and, in particular, a glimpse at the initial electron wavepacket, we performed a differential analysis by subtracting the photoelectron distributions of the two alignment cases from each other. Fig. 3 a, b, c show the relative normalised differences, parallel minus perpendicular, for the experiment, the TDDFT simulations, and the ADK-SM calculations, respectively. The agreement between experimental data and both models is excellent. Here, a strong depletion along the vertical axis and two transversely offset broad lines of positive yield appear as main features, with a really good agreement between experimental and both computational results. The depletion along the centreline is due to the nodal structure of the degenerate Π HOMO of OCS: it represents a forbidden direction of electron ejection [18, 40]. Therefore, when the molecular axis was aligned along the polarisation axis of the strong field, the electron preferentially acquired an initial transverse momentum p_{0X} that was much larger than in the case of perpendicular alignment, shown by the red vertical ridges in Fig. 3 a, b, c.

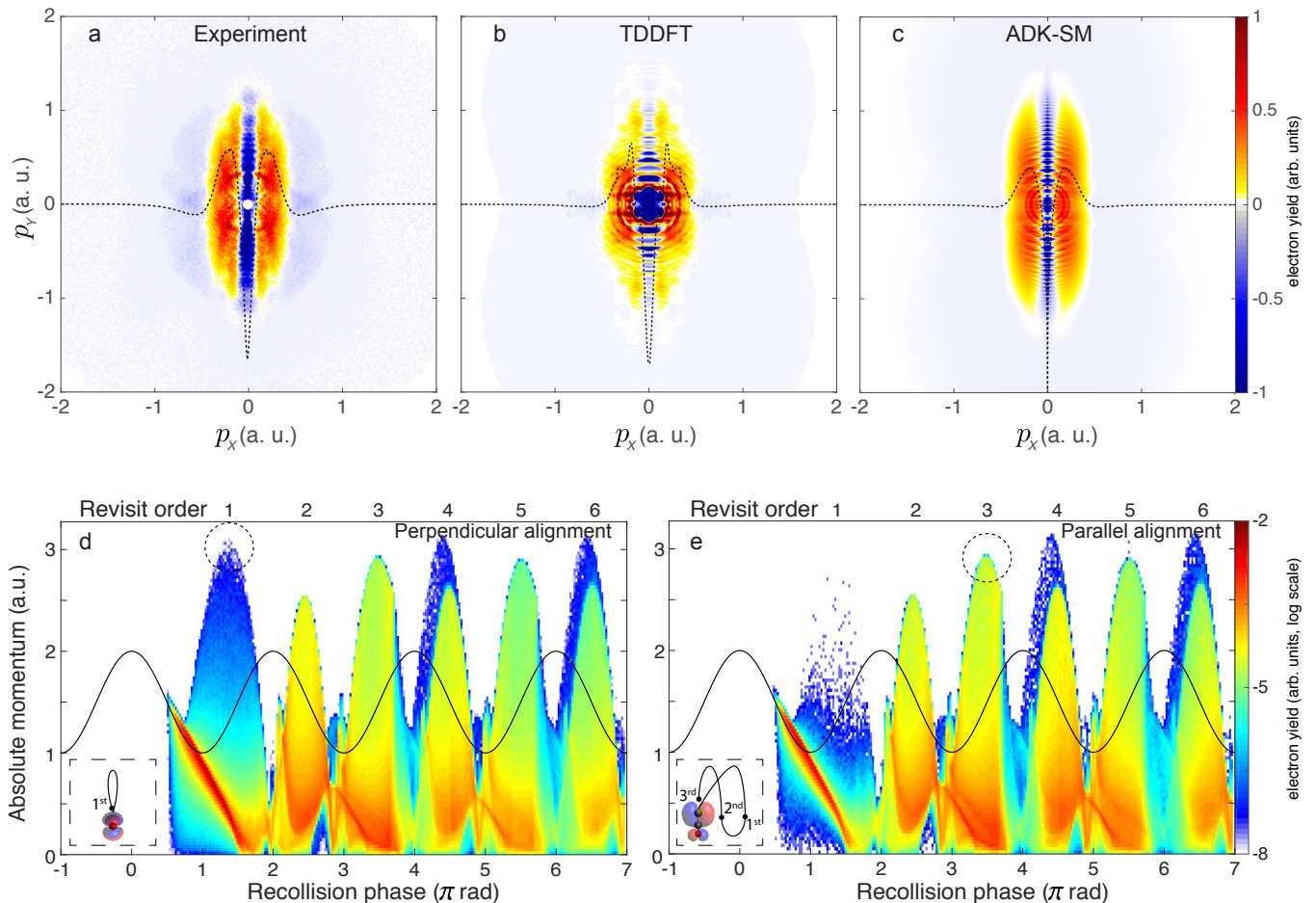


FIG. 3. Differential momentum distributions and simulated final absolute photoelectron momentum. **a, b, c**: Differential momentum distributions (parallel-perpendicular) from **a** the experiment and the **b** TDDFT and **c** ADK-SM calculations. To estimate the difference of the transverse momentum component the signal is integrated along the Y axis, shown by the black dashed lines. **d, e**: Final absolute photoelectron momentum as a function of the recollision phase (bottom) and revisit order (top) for **d** perpendicular and **e** parallel alignment, calculated with ADK-SM. The colour scale maps the electron counts at every momentum-phase point. The dashed black circles highlight the largest-momentum electrons at the most probable revisit order for the two alignments. A distance of $r < 5$ atomic units between electron and point charge is interpreted as a collision and only electrons with exactly one collision are shown. The solid black line depicts the external electric field. The insets give pictorial representations of molecular-frame electron trajectories, where the cardinals represent the revisit order.

DISCUSSION

The features observed in Fig. 3 a, b, c show the crucial impact of the electronic structure on the initial conditions of the electron at birth. However, a quantitative evaluation of the initial conditions of the electron at tunnelling is challenging [41–43]. In general, they are defined by the tunnel-exit position as well as by the temporal phase and the momentum acquired during the ionisation with respect to the external field. Here, we demonstrate that the molecular potential, i. e., the combination of the electrostatic potential and the electronic structure of the molecule, has in fact not only a primary role in setting the initial conditions for electron emission, but that it also drives the whole photoelectron dynamics: it defines

the cutoff of rescattered electrons and it shapes the time-energy relation for electron recollision. To investigate this, we exploited the ADK-SM calculations to analyse the final absolute momentum acquired by the electron after photoionisation as a function of the recollision phase. In the following discussion we will refer to revisit to describe passages of the electron nearby the cation on a relatively large spatial scale, where momentum transfer is relatively small and soft, whereas recollision, or rescattering, refers to the close approach of the electron to a nucleus, with an associated large momentum transfer, e. g., in back scattering. While multiple revisits may occur during the interaction of the electron with its cation, a recollision event will drive the electron irreversibly away from the molecule. The resulting momentum distribu-

tions are reported in Fig. 3 d, e for perpendicular and parallel alignment, respectively. They consist of broad peaks appearing every half cycle of the electric field at phases close to $(k + 1/2)\pi$, $k = 1, 2, 3 \dots$, for which the electron collides with the molecular cation when the laser field's vector potential is maximum. The first recollision event, i. e., the first peak in Fig. 3 d at a phase of $3\pi/2$, allows the electron to reach the largest momentum as expected in the classical theory [29]. This is close to the maximum asymptotic kinetic energy, i. e., the $10 U_p$ cutoff. The peaks appearing later correspond to electrons that have initially missed and then revisited the ion at later times. These subsequent rescattering events are expected to lead to lower photoelectron energies [29]. At the same time, these multiple revisits are possible only due to the Coulomb attraction of the ionised molecule [29]. Since the current understanding and analysis of strong-field self-diffraction experiments only consider the photoelectron recollision on the first revisit [7, 12], the relevance of Coulomb attraction is usually neglected. However, our results demonstrate that it is a crucial ingredient to correctly understand molecular-frame electron rescattering. Note that a small yield at large momentum (> 3 a. u.) is visible for both alignments, Fig. 3 d, e, at the fourth and the sixth revisit. These revivals, caused by Coulomb focussing, *vide supra* [39], are expected to vanish for imperfect linear polarisation of the laser field, as usually occurring in any experiment. This explains why ADK-SM for parallel alignment has another cutoff around $10.7 U_p$, as well as the more pronounced cutoff around $9.3 U_p$ in Fig. 2 i. Due to the subtle conditions of Coulomb focussing, this effect will not be further considered in the discussion below; it does not contradict any of our general conclusions.

In this framework, the largest absolute momentum for perpendicular alignment comes from the first rescattering event at a phase around $3\pi/2$, see Fig. 3 d and its inset, which yields the largest momentum ~ 3.15 a. u.. This momentum corresponds to an asymptotic kinetic energy $\sim 10.5 U_p$ and thus explains the experimental observation of the $10 U_p$ cutoff for perpendicular alignment, see the red marker in Fig. 2 c. This rescattering event is attenuated by the imprinting of the nodal plane perpendicular to the molecular axis [17], as otherwise this first peak would not only correspond to the largest photoelectron momentum, but also to the most probable recollision event. This attenuation for perpendicular alignment is responsible for the rescattering at the third revisit, i. e., at a phase around $7\pi/2$, to play a major role at lower energies and for the build up of a secondary cutoff at $\sim 9 U_p$, Fig. 2 i. While this second distinct minimum is not clearly visible in the first derivative of the experiment and the TDDFT calculations, i. e., the red curves in Fig. 2 c, f, the broad shape of the minima in Fig. 2 c, f at high energy may be in fact a signature of the attenuation of the scattering at first revisit and the relevant contribution of the third

revisit. In the case of parallel alignment, instead, the first rescattering event is strongly suppressed and most of the large-momentum electrons come from the third revisit at a phase of $7\pi/2$, depicted in the inset of Fig. 3 e; the fifth revisit also yields comparable momenta. As a result, the momentum cutoff is smaller, i. e., ~ 2.9 a. u., corresponding to a final kinetic energy of $\sim 9 U_p$. This is in good agreement with the experimentally observed reduced cutoff for parallel alignment, see the blue marker in Fig. 2 c and Fig. 2 f, i. This dynamics is mainly driven by the molecular potential: Here, the node of the HOMO along the laser polarisation imprints an angle on the electron emission at tunnelling. For OCS this angle was estimated to be $\sim 30^\circ$ with respect to the longitudinal Y axis by the TDDFT calculations. This angle prevents the electron from rescattering at the first revisit. However, then the Coulomb attraction of the ionised molecule forces the electron to stay in the interaction region and to recollide at later revisits. It is important to note that the angle of emission and the rescattering at the n -th revisit are strongly correlated. Indeed, larger emission angles lead to later revisits and *vice versa*. As the consequence, the photoelectron cutoff carries a clear signature of the electronic structure at tunnelling. This angular dependence imprinted in the momentum distribution of the initial electron wavepacket leads to the breakdown [17] of the common product ansatz in QRS [15], where the initial and the rescattered parts of the wavepacket are separated and only the latter is considered angularly dependent in the recollision frame.

Furthermore, the photoelectron cutoff in the molecular frame carries crucial time information: While the cutoff for perpendicular alignment is strongly shaped by electrons recolliding $3/4$ of an optical cycle after ionisation, as usually assumed, this is not true for parallel alignment: the cutoff is dominated by electrons revisiting the molecule much later, namely one or multiple optical cycles later. For a wavelength of 1300 nm this corresponds, at least, to a delay of ~ 4.3 fs and it linearly increases with the wavelength. From Fig. 3 d, e, apart from the aforementioned effects of Coulomb focussing, it is also evident that even-numbered revisits yield lower kinetic energies $< 8 U_p$ [29]. Since the time spent by the photoelectron before rescattering is usually exploited as the elementary delay step for time-resolved self-diffraction experiments [7], the use of this lower range of photoelectron energy [9, 12] results in any time information being smeared out on much longer timescales. Furthermore, the analysis performed here demonstrated that this delay step strongly depends on the molecular-frame alignment and that the molecular potential sets a complex time-energy encoding in the electron dynamics. This molecular-frame clock for electron recollision could clearly be exploited to disentangle the structural dynamics with few-fs or even sub-fs temporal resolution. For instance, signals from the first (few) revisit order(s) could be selected in the

experiment with near-single-cycle (few-cycle) laser pulses.

We demonstrated, experimentally and computationally, that the molecular frame determines the momentum distribution of high-energy rescattered electrons in strong-field ionisation. The basic concept of molecular-frame strong-field ionisation is captured by considering the initial conditions imposed by the molecular potential in the dynamics of the photoelectron. Furthermore, from the analysis of the rescattering trajectories it is evident that the molecular interaction plays a crucial role in setting a clock for the emission and the dynamics of high-energy electrons. It highlights that the molecular frame has a strong impact on the relation between the photoelectron energy and the rescattering time. This finding redefines the delay step of time-resolved self-diffraction experiments and opens up a perspective on time-resolved diffraction experiments. These conclusions hold similarly for other observables related to electron recollision, e. g., high-harmonic-generation spectroscopy.

Our result represents an important benchmark for any self-diffraction measurement and represents a breakdown of the usual interpretation of LIED experiments [7, 9, 12]. We note that in such experiments mid-infrared lasers ($\lambda \approx 3 \mu\text{m}$) are typically employed. Since the electron’s excursion length increases with increasing laser wavelengths, we expect our findings to be even more relevant for actual LIED experiments.

Our study highlights the molecular-frame conditions as a crucial ingredient of self-diffraction experiments. This framework is general and can, in principle, be extended to any molecular system. Furthermore, the molecular-frame strong-field interaction was quantitatively modelled here by a fully-interacting-electron TDDFT calculation and, in conjunction, by a semiclassical single-active-electron theory. We exploited TDDFT to evaluate the contribution of different molecular orbitals to the ionisation-rescattering dynamics as a benchmark for the applicability of the semiclassical approach. We expect this double-sided theoretical framework to become more and more important with increasing molecular complexity, where modelling the photoelectron dynamics may go beyond the capabilities of a single-orbital picture. In general, this also opens the perspective to investigate electron-correlation-driven phenomena in molecular strong-field physics [4]. Furthermore, the earliest moments of a strong-field interaction are intrinsically imprinted in the initial conditions of the photoelectron and in the final energy distribution. Thus, molecular-frame strong-field-ionisation experiments, in principle, allow one to achieve a deeper understanding of electron tunnelling, for instance, regarding the tunnelling time, and to track the molecular potential in real-time.

ACKNOWLEDGEMENTS

This work has been supported by the Clusters of Excellence “Center for Ultrafast Imaging” (CUI, EXC 1074, ID 194651731) and “Advanced Imaging of Matter” (AIM, EXC 2056, ID 390715994) of the Deutsche Forschungsgemeinschaft (DFG), by the European Research Council under the European Union’s Seventh Framework Programme (FP7/2007-2013) through the Consolidator Grant COMOTION (ERC-Küpper-614507) and under the Horizon 2020 Research and Innovation Programme through the Advanced Grant QSpec-NewMat (ERC-Rubio-694097), and by the Helmholtz Association Initiative and Networking Fund. A.T. and J.O. gratefully acknowledge fellowships by the Alexander von Humboldt Foundation.

AUTHOR CONTRIBUTIONS

A.T., S.T., and J.K. conceived the experiment. A.T., S.T., J.F.O., J.W., T.M., and J.O. performed the experiment. A.T. performed the data analysis. J.W. set up and performed the ADK-SM simulations. U.D.G. and B.F. performed the TDDFT calculations, and together with S.-K.S. and A.R. provided theoretical support. A.T., S.T., U.D.G., J.W., A.R., and J.K. interpreted the results and prepared the manuscript. All authors contributed to the discussion of the results and commented on the manuscript.

Correspondence and requests for materials should be addressed to A.R. (angel.rubio@mpsd.mpg.de) and J.K. (jochen.kuepper@cfel.de).

Appendix A: Numerical quantum-dynamics simulations

Numerical simulations of the full LIED dynamics have been performed from first-principles within the time-dependent density functional theory (TDDFT) [32] framework as implemented in the real-space real-time Octopus code [44]. In TDDFT, the dynamics of an interacting many-electron system is cast into the manageable problem of a fictitious non-interacting system under the effect of a time-dependent potential such that the non-interacting and the interacting systems have the same time-dependent density.

Since core electrons are expected to play a marginal role in the experiment we consider only valence electrons and account for inner-shell electrons by the effect of norm-conserving Troullier-Martins pseudopotentials. To obtain a good description of ionisation, we employed a local density approximation (LDA) functional with the average density self-interaction correction (ADSIC) [45], which corrects the asymptotic decay and provides a first and second ionisation energy of 11.65 eV and 15.69 eV, in

good agreement with experimental values [46]. During the simulations the nuclei are held fixed in the equilibrium positions, $r_{C-S} = 156.1$ pm and $r_{C-O} = 115.6$ pm.

The TDDFT equations are discretised in real-space with a cartesian grid of spacing 0.4 a. u. with a cylindrical shape of radius 50 a. u. and length 260 a. u. aligned along the laser-polarisation direction. The solution of the electron dynamics is obtained by using a discretised real-time evolution with a time step of 0.08 a. u.. The calculations are performed with a 30 fs laser pulse. Complex absorbing boundaries of varying thicknesses, 40 a. u. from the caps of the cylinder and 10 a. u. on the radial borders, are placed at the edges of the simulation box to prevent spurious reflections [47].

The photoelectron spectrum is calculated by collecting the flux of the photoionisation current through a spherical surface of radius 40 a. u. with the tSURFF method [33, 34]. This approach gives access to the momentum resolved photoelectron probability $I(\mathbf{p})$ from which, by integrating along the direction perpendicular to the detector, it is possible to obtain the angular distribution of the experiment: $I(p_X, p_Y) = \int dp_Z I(\mathbf{p})$.

The non-perfect molecular alignment in the laboratory frame is accounted for by sampling the relative angle θ between the laser polarisation and the molecular axis from 0° to 90° in steps of 10° , as shown in Supplementary Figure 1. This procedure requires a separate simulation for each θ . The photoelectron spectra for a given configuration, parallel or perpendicular, are obtained by averaging the photoelectron distributions $I_\theta(\mathbf{p})$ with weights $n_\theta(\theta - \theta^{\parallel/\perp}) = \exp(-\sin(\theta - \theta^{\parallel/\perp})^2/(2\sigma^2))$, $\sigma^2 = 1 - \langle \cos^2\theta_{2D} \rangle$, and $\langle \cos^2\theta_{2D} \rangle = 0.9$.

Furthermore, to account for the rotation of the molecule about the polarisation axis for parallel alignment we impose cylindrical symmetry of the photoelectron distribution about Y by averaging over ϕ : $\bar{I}_\phi(\mathbf{p}) = (2\pi)^{-1} \int_0^{2\pi} d\phi R_\phi(I(\mathbf{p}))$ with the operator R_ϕ of rotation in the X, Z plane. The final spectrum is obtained as follows:

$$\bar{I}^{\parallel/\perp}(p_X, p_Y) = \int dp_z \int d\theta n(\theta - \theta^{\parallel/\perp}) \bar{I}_{\phi, \theta}(\mathbf{p}). \quad (1)$$

To account for experimental-background in the simulations, a constant offset of 2×10^{-8} was added to the energy distributions, see Supplementary Figure 2. For comparison, the spectra for perfectly aligned configurations are reported in Supplementary Figure 3. We point out that the background correction shifts the numerically obtained cutoffs to lower energy, but does not affect the general behaviour nor the difference of the cutoffs between the parallel and perpendicular configurations.

From the numerical simulations the crucial role of the usually neglected electron-electron interaction for correctly describing the cutoff region in the parallel configuration became evident. Supplementary Figure 4 a shows the decomposed contributions of the Kohn-Sham HOMO

and HOMO-1 orbitals, which highlight their distinct contributions to two distinct cutoffs, which are strongly separated in intensity. In particular, the faint $10 U_p$ cutoff for the parallel case actually appears to be uniquely determined by the HOMO-1, which does not have a node along the molecular axis, whereas contributions from the HOMO were strongly suppressed by the presence of a node along the molecular axis, i. e., parallel to the laser-polarisation axis. Second, the independent particle simulation obtained by propagating the system with the Hartree, exchange, and correlation potentials frozen, mimicking the widely used single-active electron model, presents a qualitatively different picture, see Supplementary Figure 4 b. In particular the contribution of the HOMO-1 is highly overestimated and for the parallel alignment the $10 U_p$ cutoff is restored, in clear contradiction with the experiment. These results also confirm the importance of the coherent interaction between different orbitals in strong-field ionisation [48].

Appendix B: Semiclassical trajectory simulations

Semiclassical trajectory simulations were carried out employing a simplified MO-ADK (molecular-orbital Ammosov-Delone-Kraĭnov) approach, to create the initial wavepacket, in conjunction with a classical continuum propagation in the combined laser-electric and Coulomb field of the cation.

Initial electron wavepacket

In general, the phase-space distribution of the initial electron wavepacket was created in a similar fashion as described before [40]. The ionisation probability in dependence of the instantaneous electric field was obtained through the quasistatic ADK tunnelling theory supplemented by an empirical extension to the barrier-suppression regime [49]. Electric-field dependent ionisation potentials, $I_p(\vec{\epsilon})$, were computed through second-order perturbation theory

$$I_p(\vec{\epsilon}) = I_p^{(0)} - \Delta\vec{\mu} \cdot \vec{\epsilon} - \frac{1}{2} \vec{\epsilon}^T \Delta\alpha \vec{\epsilon}, \quad (2)$$

assuming that ionisation occurs exclusively from the HOMO, as supported by the TDDFT results. $I_p^{(0)}$ is the field-free ionisation potential, $\Delta\vec{\mu}$ and $\Delta\alpha$ are the differences of dipole moment and polarizability tensor between cationic and neutral species, respectively. Here, the measured field-free ionisation potential of $I_p^{(0)} = 11.19$ eV [46] was used in combination with calculated neutral and cationic dipole moments and polarizabilities [40]. In Supplementary Figure 5 the resulting time-of-birth distribution of a typical electron wavepacket is shown.

The classical tunnel exit was composed as $\vec{r}_0 = -\vec{c}I_p/\epsilon^2$ [50]. The initial momentum distribution in the plane transverse to the electric field vector at the instance of ionisation was modelled according to the atomic ADK tunnelling theory with additional imprint of the initial electronic state's nodal structure. The initial momentum component along the electric field vector was obtained through nonadiabatic tunnelling theory [51]. For the parallel-alignment case the nodal line of the HOMOs along the molecular axis imprints onto the momentum distribution at birth. Accordingly, the initial transverse momentum distribution for the parallel alignment case was described as

$$\omega_{\parallel}(p_{0,x}, p_{0,z}) \propto (p_{0,x}^2 + p_{0,z}^2) \cdot e^{-\frac{\sqrt{2I_p}}{\epsilon}(p_{0,x}^2 + p_{0,z}^2)}. \quad (3)$$

For the perpendicular alignment case the nodal plane orthogonal to the molecular axis imprints onto the initial momentum distribution. Since it splits the HOMO's electron density unequally with a ratio of 85:15 [40], its imprint was described as a nodal plane with a damped peculiarity

$$\beta = 1 - \frac{|\varrho_+ - \varrho_-|}{\varrho_+ + \varrho_-}, \quad (4)$$

with ϱ_{\pm} representing the integral electron densities on the two sides of the nodal plane. Hence, the distribution of initial transverse momenta for the perpendicular alignment case was set up as

$$\omega_{\perp}(p_{0,x}, p_{0,z}) \propto |p_{0,z}|^{2\beta} \cdot e^{-\frac{\sqrt{2I_p}}{\epsilon}(p_{0,x}^2 + p_{0,z}^2)}. \quad (5)$$

Supplementary Figure 6 illustrates exemplary transverse momentum distributions for both alignment cases.

Classical propagation

The electron wavepacket at birth into the continuum was sampled from the initial phase-space distribution through rejection sampling, expanded as a coherent superposition of partial plane waves and, subsequently, propagated in the combined electric laser and the cation's Coulomb field. The singly charged cation was represented by a point charge $+e$.

The asymptotic electron phase after exposure to the combined electric field of laser and point charge was obtained through [52]

$$\phi_{\infty} = -\vec{p}_0 \cdot \vec{r}_0 + I_p \cdot t_0 - \int_{t_0}^{\infty} \left(\frac{p^2}{2} - \frac{2}{r} \right) dt. \quad (6)$$

At short distances between the electron and the point charge, $r < r_{2b}$, the laser-electric field becomes negligible and the description of the electron motion reduces to

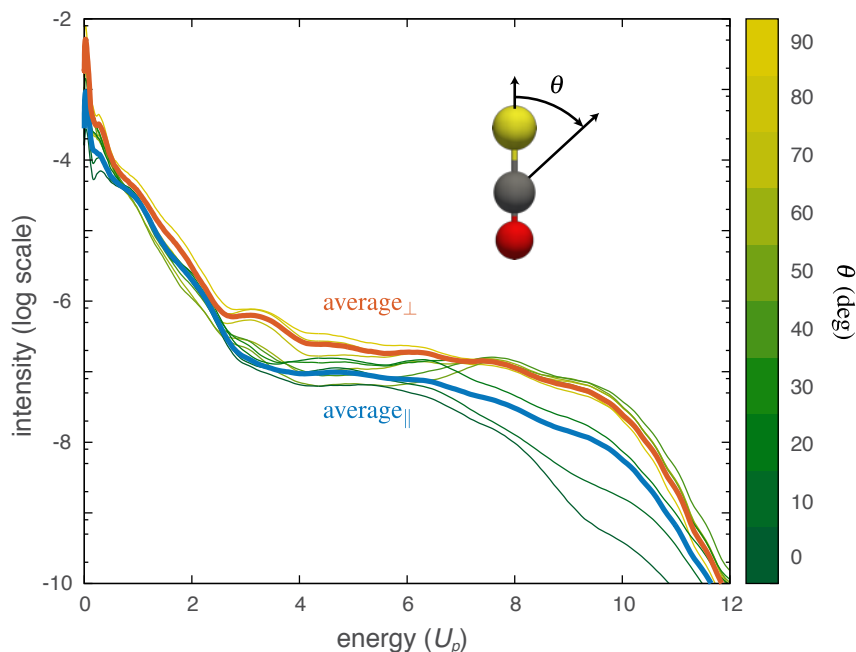
a two-body problem. Here, the threshold distance, r_{2b} , was chosen such that the corresponding Coulomb field is 1000 times larger than the peak electric field of the laser. Accordingly, for the experimental peak electric field of $\epsilon_0 \approx 0.048$ a. u. this threshold distance becomes $r_{2b} = 1/\sqrt{1000\epsilon_0} \approx 0.14$ a. u.. The motion of the electron within the spherical volume of radius r_{2b} around the point charge could then be described conveniently as a Kepler orbit. This approximation allows for direct computation of the electron's properties at its symmetric exit point from the sphere: Its position and momentum vector at exit as well as its time of flight between entry and exit of this sphere can be computed fully analytically. The phase accumulated during its passage through the sphere is accessible through low-effort numerical integration. In Supplementary Figure 7 a typical trajectory of an electron is shown as it performs a swing-by around the point charge.

-
- [1] P. B. Corkum, "Plasma perspective on strong-field multiphoton ionization," *Phys. Rev. Lett.* **71**, 1994–1997 (1993).
 - [2] P. B. Corkum, M. Y. Ivanov, and J. S. Wright, "Sub-femtosecond processes in strong laser fields," *Annu. Rev. Phys. Chem.* **48**, 387–406 (1997).
 - [3] F. Calegari, D. Ayuso, A. Trabattoni, L. Belshaw, S. De Camillis, S. Anumula, F. Frassetto, L. Poletto, A. Palacios, P. Decleva, J. B. Greenwood, F. Martín, and M. Nisoli, "Ultrafast electron dynamics in phenylalanine initiated by attosecond pulses," *Science* **346**, 336–339 (2014).
 - [4] F. Lépine, M. Y. Ivanov, and M. J. J. Vrakking, "Attosecond molecular dynamics: fact or fiction?" *Nat. Photon.* **8**, 195–204 (2014).
 - [5] P. M. Kraus, B. Mignolet, D. Baykusheva, A. Rupenyan, L. Horný, E. F. Penka, G. Grassi, O. I. Tolstikhin, J. Schneider, F. Jensen, L. B. Madsen, A. D. Bandrauk, F. Remacle, and H. J. Wörner, "Measurement and laser control of attosecond charge migration in ionized iodoacetylene," *Science* **350**, 790–795 (2015).
 - [6] P. B. Corkum and F. Krausz, "Attosecond Science," *Nat. Phys.* **3**, 381–387 (2007).
 - [7] C. I. Blaga, J. Xu, A. D. DiChiara, E. Sistrunk, K. Zhang, P. Agostini, T. A. Miller, L. F. DiMauro, and C. D. Lin, "Imaging ultrafast molecular dynamics with laser-induced electron diffraction," *Nature* **483**, 194–197 (2012).
 - [8] M. G. Pullen, B. Wolter, A.-T. Le, M. Baudisch, M. Hemmer, A. Senftleben, C. D. Schroter, J. Ullrich, R. Moshhammer, C. D. Lin, and J. Biegert, "Imaging an aligned polyatomic molecule with laser-induced electron diffraction," *Nat. Commun.* **6**, 7262 (2015).
 - [9] B. Wolter, M. G. Pullen, A. T. Le, M. Baudisch, K. Doblhoff-Dier, A. Senftleben, M. Hemmer, C. D. Schroter, J. Ullrich, T. Pfeifer, R. Moshhammer, S. Gräfe, O. Vendrell, C. D. Lin, and J. Biegert, "Ultrafast electron diffraction imaging of bond breaking in di-ionized acetylene," *Science* **354**, 308–312 (2016).
 - [10] S. G. Walt, B. N. Ram, M. Atala, N. I. Shvetsov-Shilovski,

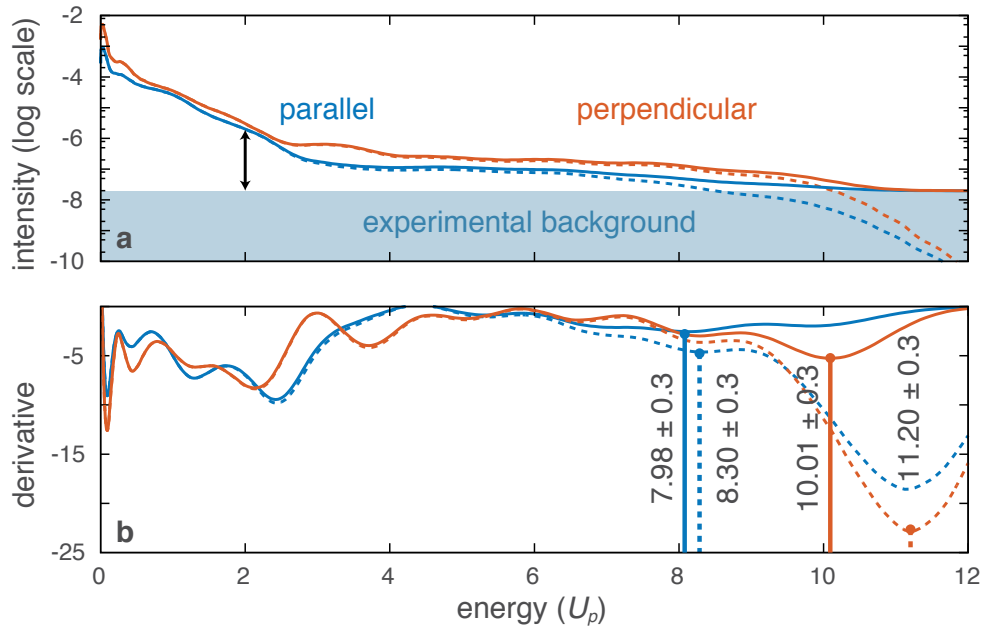
- A. von Conta, D. Baykusheva, M. Lein, and H. J. Wörner, “Dynamics of valence-shell electrons and nuclei probed by strong-field holography and rescattering,” *Nat. Commun.* **8**, 15651 (2017).
- [11] H. Fuest, Y. H. Lai, C. I. Blaga, K. Suzuki, J. Xu, P. Rupp, H. Li, P. Wnuk, P. Agostini, K. Yamazaki, M. Kanno, H. Kono, M. F. Kling, and L. F. DiMauro, “Diffractive imaging of c60 structural deformations induced by intense femtosecond midinfrared laser fields,” *Phys. Rev. Lett.* **122**, 053002 (2019).
- [12] K. Amini, M. Sclafani, T. Steinle, A.-T. Le, A. Sanchez, C. Müller, J. Steinmetzer, L. Yue, J. R. M. Saavedra, M. Hemmer, M. Lewenstein, R. Moshhammer, T. Pfeifer, M. G. Pullen, J. Ullrich, B. Wolter, R. Moszynski, F. J. G. de Abajo, C. D. Lin, S. Gräfe, and J. Biegert, “Imaging the Renner–Teller effect using laser-induced electron diffraction,” *PNAS* **116**, 8173 (2019).
- [13] P. Eckle, A. N. Pfeiffer, C. Cirelli, A. Staudte, R. Dörner, H. G. Muller, M. Büttiker, and U. Keller, “Attosecond ionization and tunneling delay time measurements in helium,” *Science* **322**, 1525–1529 (2008).
- [14] M. Meckel, A. Staudte, S. Patchkovskii, D. M. Villeneuve, P. B. Corkum, R. Dörner, and M. Spanner, “Signatures of the continuum electron phase in molecular strong-field photoelectron holography,” *Nat. Phys.* **10**, 594–600 (2014).
- [15] Z. Chen, A.-T. Le, T. Morishita, and C. D. Lin, “Quantitative rescattering theory for laser-induced high-energy plateau photoelectron spectra,” *Phys. Rev. A* **79**, 033409 (2009).
- [16] J. Xu, C. I. Blaga, K. Zhang, Y. H. Lai, C. D. Lin, T. A. Miller, P. Agostini, and L. F. DiMauro, “Diffraction using laser-driven broadband electron wave packets,” *Nat. Commun.* **5**, 4635 (2014).
- [17] F. Schell, T. Bredtmann, C.-P. Schulz, S. Patchkovskii, M. J. J. Vrakking, and J. Mikosch, “Molecular orbital imprint in laser-driven electron recollision,” *Science Advances* **4**, eaap8148 (2018).
- [18] M. Lein, “Antibonding molecular orbitals under the influence of elliptically polarized intense light,” *J. Phys. B* **36**, L155 (2003).
- [19] H. Niikura, F. Legare, R. Hasbani, A. D. Bandrauk, M. Y. Ivanov, D. M. Villeneuve, and P. B. Corkum, “Sub-laser-cycle electron pulses for probing molecular dynamics,” *Nature* **417**, 917–922 (2002).
- [20] M. Busuladžić, A. Gazibegović-Busuladžić, D. B. Milošević, and W. Becker, “Angle-resolved high-order above-threshold ionization of a molecule: Sensitive tool for molecular characterization,” *Phys. Rev. Lett.* **100**, 203003 (2008).
- [21] M. G. Pullen, B. Wolter, A. T. Le, M. Baudisch, M. Sclafani, H. Pires, C. D. Schröter, J. Ullrich, R. Moshhammer, T. Pfeifer, C. D. Lin, and J. Biegert, “Influence of orbital symmetry on diffraction imaging with rescattering electron wave packets,” *Nat. Commun.* **7**, 11922 (2016).
- [22] N. Suárez, A. Chacón, M. F. Ciappina, B. Wolter, J. Biegert, and M. Lewenstein, “Above-threshold ionization and laser-induced electron diffraction in diatomic molecules,” *Phys. Rev. A* **94**, 043423 (2016).
- [23] M.-M. Liu, M. Li, C. Wu, Q. Gong, A. Staudte, and Y. Liu, “Phase structure of strong-field tunneling wave packets from molecules,” *Phys. Rev. Lett.* **116**, 163004 (2016).
- [24] Y.-P. Chang, D. A. Horke, S. Trippel, and J. Küpper, “Spatially-controlled complex molecules and their applications,” *Int. Rev. Phys. Chem.* **34**, 557–590 (2015), arXiv:1505.05632 [physics].
- [25] S. Trippel, T. Mullins, N. L. M. Müller, J. S. Kienitz, K. Długołęcki, and J. Küpper, “Strongly aligned and oriented molecular samples at a kHz repetition rate,” *Mol. Phys.* **111**, 1738 (2013), arXiv:1301.1826 [physics].
- [26] S. Trippel, T. Mullins, N. L. M. Müller, J. S. Kienitz, J. J. Omiste, H. Stapelfeldt, R. González-Férez, and J. Küpper, “Strongly driven quantum pendulum of the carbonyl sulfide molecule,” *Phys. Rev. A* **89**, 051401(R) (2014), arXiv:1401.6897 [quant-ph].
- [27] A. T. J. B. Eppink and D. H. Parker, “Velocity map imaging of ions and electrons using electrostatic lenses: Application in photoelectron and photofragment ion imaging of molecular oxygen,” *Rev. Sci. Instrum.* **68**, 3477–3484 (1997).
- [28] W. Becker and D. B. Milošević, “Above-threshold ionization for very low electron energy,” *J. Phys. B* **48**, 151001 (2015).
- [29] G. G. Paulus, W. Becker, W. Nicklich, and H. Walther, “Rescattering effects in above threshold ionization: a classical model,” *J. Phys. B* **27**, L703–L708 (1994).
- [30] W. Becker, F. Grasbon, R. Kopold, D. B. Milošević, G. G. Paulus, and H. Walther, “Above-threshold ionization: From classical features to quantum effects,” *Adv. Atom. Mol. Opt. Phys.* **48**, 35–98 (2002).
- [31] C. T. L. Smeenk, L. Arissian, A. V. Sokolov, M. Spanner, K. F. Lee, A. Staudte, D. M. Villeneuve, and P. B. Corkum, “Alignment dependent enhancement of the photoelectron cutoff for multiphoton ionization of molecules,” *Phys. Rev. Lett.* **112**, 253001 (2014), arXiv:1304.6942 [physics].
- [32] M. A. L. Marques, N. T. Maitra, F. Nogueira, E. K. U. Gross, and A. Rubio, *Fundamentals of Time-Dependent Density Functional Theory*, Lecture Notes in Physics (Springer Verlag, 2011).
- [33] L. Tao and A. Scrinzi, “Photo-electron momentum spectra from minimal volumes: the time-dependent surface flux method,” *New J. Phys.* **14**, 013021 (2012).
- [34] P. Wopperer, U. De Giovannini, and A. Rubio, “Efficient and accurate modeling of electron photoemission in nanostructures with TDDFT,” *Eur. Phys. J. D* **90**, 1307 (2017).
- [35] M. V. Ammosov, N. B. Delone, and V. P. Krainov, “Tunnel ionization of complex atoms and of atomic ions in an alternating electromagnetic field,” *Soviet Physics - JETP* **64**, 1191–1194 (1986).
- [36] T. F. Gallagher, “Above-threshold ionization in low-frequency limit,” *Phys. Rev. Lett.* **61**, 2304–2307 (1988).
- [37] P. B. Corkum, N. H. Burnett, and F. Brunel, “Above-threshold ionization in the long-wavelength limit,” *Phys. Rev. Lett.* **62**, 1259–1262 (1989).
- [38] J. Wiese, J. Onvlee, S. Trippel, and J. Küpper, “Strong-field ionization of complex molecules,” (2020), arXiv:2003.02116 [physics].
- [39] J. Daněk, M. Klaiber, K. Z. Hatsagortsyan, C. H. Keitel, B. Willenberg, J. Maurer, B. W. Mayer, C. R. Phillips, L. Gallmann, and U. Keller, “Interplay between Coulomb-focusing and non-dipole effects in strong-field ionization with elliptical polarization,” *J. Phys. B* **51**, 114001 (2018).
- [40] L. Holmegaard, J. L. Hansen, L. Kalhøj, S. L. Kragh, H. Stapelfeldt, F. Filsinger, J. Küpper, G. Meijer, D. Dimitrovski, M. Abu-samha, C. P. J. Martiny, and L. B. Mad-

- sen, “Photoelectron angular distributions from strong-field ionization of oriented molecules,” *Nat. Phys.* **6**, 428 (2010), arXiv:1003.4634 [physics].
- [41] A. N. Pfeiffer, C. Cirelli, A. S. Landsman, M. Smolarski, D. Dimitrovski, L. B. Madsen, and U. Keller, “Probing the longitudinal momentum spread of the electron wave packet at the tunnel exit,” *Phys. Rev. Lett.* **109**, 083002 (2012).
- [42] J.-W. Geng, W.-H. Xiong, X.-R. Xiao, L.-Y. Peng, and Q. Gong, “Nonadiabatic electron dynamics in orthogonal two-color laser fields with comparable intensities,” *Phys. Rev. Lett.* **115**, 193001 (2015).
- [43] J. Tian, X. Wang, and J. Eberly, “Numerical detector theory for the longitudinal momentum distribution of the electron in strong field ionization,” *Phys. Rev. Lett.* **118**, 213201 (2017).
- [44] X. Andrade, D. Strubbe, U. De Giovannini, A. H. Larsen, M. J. T. Oliveira, J. Alberdi-Rodriguez, A. Varas, I. Theophilou, N. Helbig, M. J. Verstraete, L. Stella, F. Nogueira, A. Aspuru-Guzik, A. Castro, M. A. L. Marques, and A. Rubio, “Real-space grids and the octopus code as tools for the development of new simulation approaches for electronic systems,” *Phys. Chem. Chem. Phys.* **17**, 31371 (2015).
- [45] C. Legrand, E. Suraud, and P. G. Reinhard, “Comparison of self-interaction-corrections for metal clusters,” *J. Phys. B-Atom. Mol. Opt.* **35**, 1115 (2002).
- [46] L. S. Wang, J. E. Reutt, Y. T. Lee, and D. A. Shirley, “High-resolution UV photoelectron-spectroscopy of CO_2^+ , COS^+ and CS_2^+ using supersonic molecular-beams,” *J. Electron. Spectrosc. Relat. Phenom.* **47**, 167–186 (1988).
- [47] U. De Giovannini, A. H. Larsen, and A. Rubio, “Modeling electron dynamics coupled to continuum states in finite volumes with absorbing boundaries,” *Eur. Phys. J. D* **88**, 1–12 (2015).
- [48] H. Akagi, T. Otobe, A. Staudte, A. Shiner, F. Turner, R. Dörner, D. Villeneuve, and P. Corkum, “Laser tunnel ionization from multiple orbitals in HCl,” *Science* **325**, 1364–1367 (2009).
- [49] X. M. Tong and C. D. Lin, “Empirical formula for static field ionization rates of atoms and molecules by lasers in the barrier-suppression regime,” *J. Phys. B* **38**, 2593–2600 (2005).
- [50] X.-B. Bian, Y. Huismans, O. Smirnova, K.-J. Yuan, M. J. J. Vrakking, and A. D. Bandrauk, “Subcycle interference dynamics of time-resolved photoelectron holography with midinfrared laser pulses,” *Phys. Rev. A* **84**, 043420 (2011).
- [51] M. Li, J.-W. Geng, M. Han, M. M. Liu, L.-Y. Peng, Q. Gong, and Y. Liu, “Subcycle nonadiabatic strong-field tunneling ionization,” *Phys. Rev. A* **93**, 013402 (2016).
- [52] N. I. Shvetsov-Shilovski, M. Lein, L. B. Madsen, E. Räsänen, C. Lemell, J. Burgdörfer, D. G. Arbó, and K. Tókési, “Semiclassical two-step model for strong-field ionization,” *Phys. Rev. A* **94**, 013415 (2016).

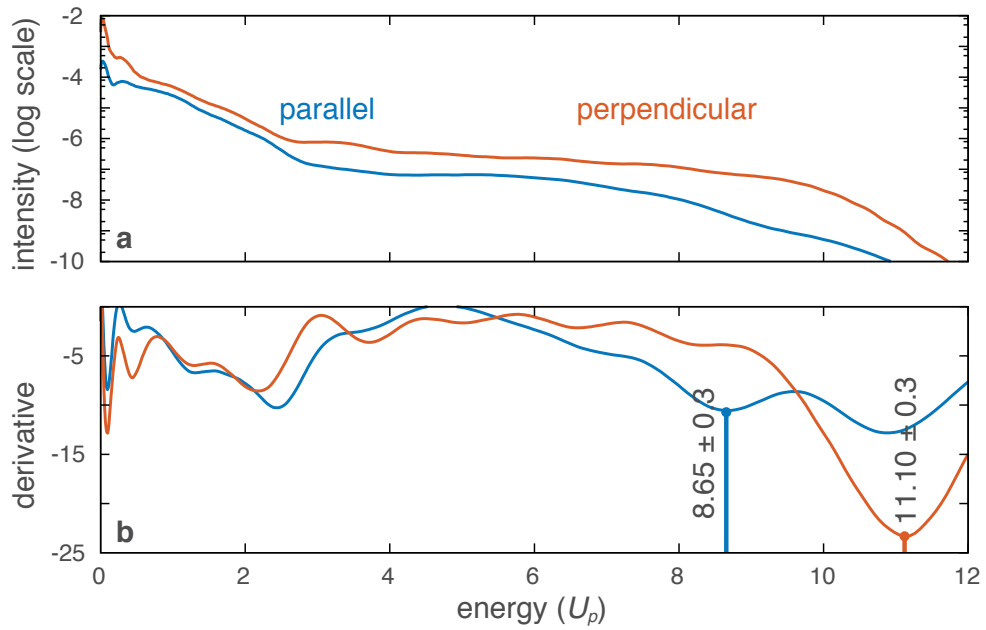
SUPPLEMENTARY FIGURES



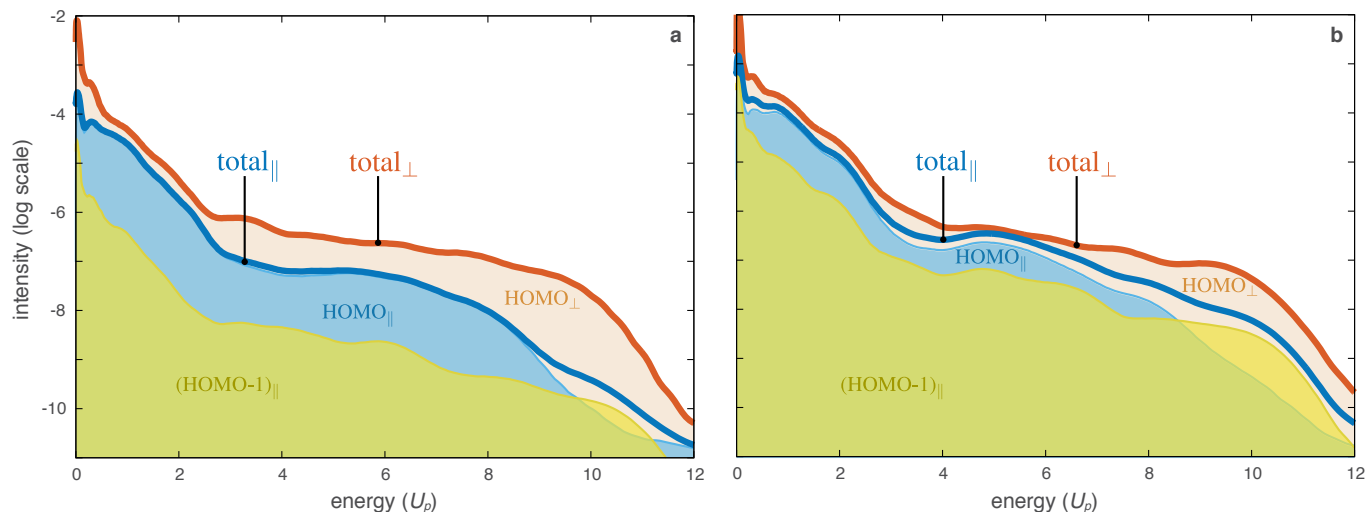
Supplementary Figure 1. Simulated photoelectron spectra as a function of the angle θ between the laser polarisation and the molecular axis. The averaged spectra for a parallel and perpendicular alignment with a degree of alignment of $\langle \cos^2 \theta_{2D} \rangle = 0.9$ are reported with thick lines.



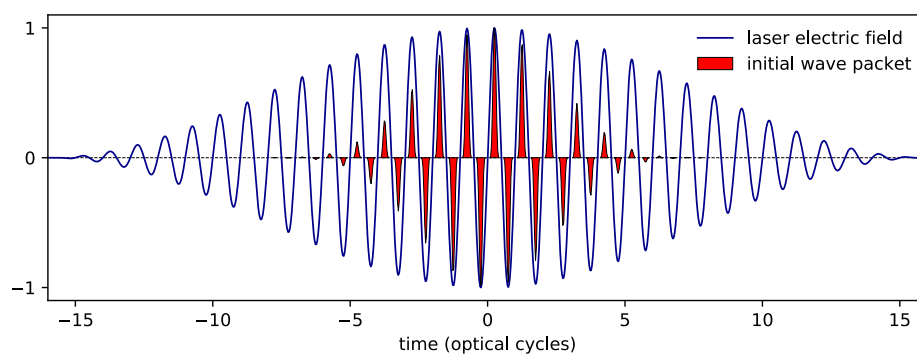
Supplementary Figure 2. Effect of the experimental-background in the simulated photoelectron spectra. **a:** Simulated photoelectron distributions, for parallel and perpendicular alignment, averaged over θ according to the degree of alignment in the experiment $\bar{I}_{\parallel/\perp}(E)$ (dashed lines). A constant, 2×10^{-8} , is added to the simulated data to account for the experimental-background level (solid lines), i. e., to match the experimental contrast from 2 to 12 U_p . **b:** Derivatives of the photoelectron distributions. Regardless of the presence of the background the cutoffs for the parallel and perpendicular configurations present an observable difference which is in qualitative agreement with the results of Fig.2 of the main manuscript.



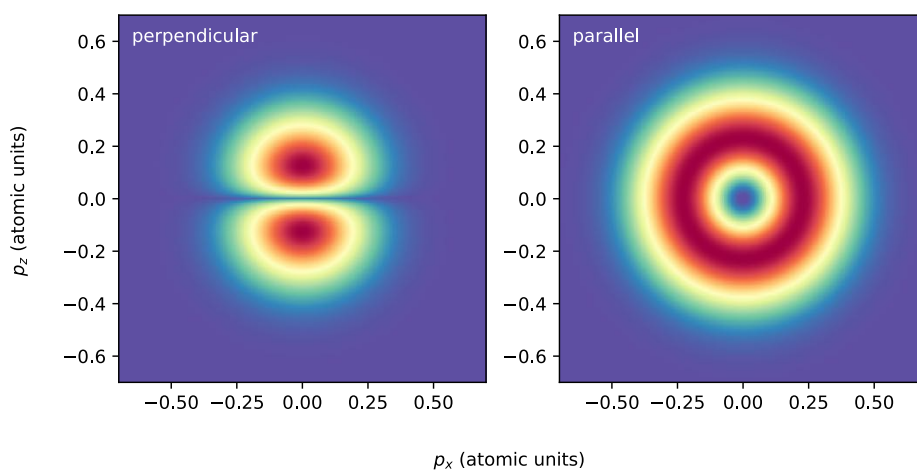
Supplementary Figure 3. Same as Supplementary Figure 2 for perfect alignment and no experimental-background correction.



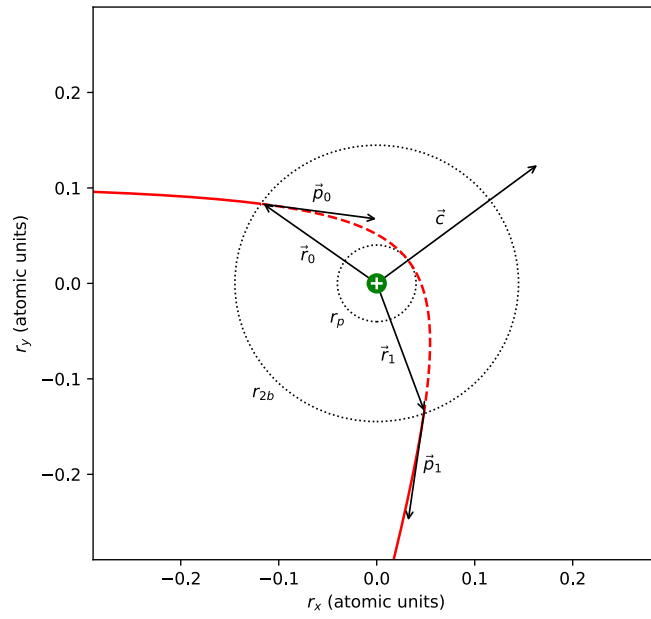
Supplementary Figure 4. Role of electron-electron interaction and orbital contribution to the total photoelectron spectrum for perfect alignment. **a:** Spectra obtained with the fully-interacting-electrons TDDFT equations. **b:** Spectra for the non-interacting-electrons simulation obtained by freezing the Hartree exchange and correlation potentials to the neutral ground state potentials.



Supplementary Figure 5. Time-of-birth distribution of an electron wavepacket for OCS at perpendicular alignment as obtained from the quasistatic ADK tunnelling theory. The distribution shown was normalised with respect to its maximum and multiplied with the sign of the instantaneous electric field. The electric field is displayed in units of ϵ_0 .



Supplementary Figure 6. Transverse initial momentum distributions assuming the field-free ionisation potential and peak electric field.



Supplementary Figure 7. Example trajectory in the combined laser-electric and Coulomb field of a point charge $+e$ (green dot), numerically propagated for $r > r_{2b}$ (solid red line) and analytically approximated for $r \leq r_{2b}$ by means of a pure two-body interaction (dashed red line). By deduction of the orbital centre \vec{c} and the distance at closest approach, the periapsis r_p , the symmetric exit position \vec{r}_1 , the corresponding momentum vector \vec{p}_1 , and the time spent within the sphere can be obtained analytically.